# A process-based analysis of Arctic Ocean warming in response to increasing CO2

**Oleg Saenko** ( oleg.a.saenko@gmail.com )
UVic: University of Victoria https://orcid.org/0000-0002-7168-7159
**Jonathan Gregory**
University of Reading Department of Meteorology
**Neil Tandon**
York University Faculty of Science and Engineering: York University Faculty of Science

**Research Article**

**Keywords:**

**Posted Date:** May 30th, 2023

**DOI:** https://doi.org/10.21203/rs.3.rs-2969020/v1



**Version of Record:** A version of this preprint was published at Climate Dynamics on November 28th, 2023. See the published version at https://doi.org/10.1007/s00382-023-06986-2.

# A process-based analysis of Arctic Ocean warming in response to increasing $CO_2$

**Oleg A. Saenko**[1,4] · **Jonathan M. Gregory**[2,3] · **Neil Tandon**[4]

Received: date / Accepted: date

**Abstract** Using an ensemble of atmosphere–ocean general circulation models (AOGCMs) in an idealized climate change experiment, this study evaluates the contribution of different ocean processes to Arctic Ocean warming. On the AOGCM-mean, the Arctic Ocean warming is greater than the global ocean warming in the volume mean, and at most depths within the upper 2000 m. The Arctic warming is greatest a few 100 m below the surface and is dominated by the import of extra heat which is added to the ocean at lower latitude and is conveyed to the Arctic via the large-scale barotropic ocean circulation. The change in strength of this circulation in the North Atlantic is relatively small and not correlated with the Arctic Ocean warming. The Arctic Ocean warming is opposed and substantially mitigated by the weakening of the Atlantic meridional overturning circulation (AMOC), though the magnitude of this effect has a large model spread. By reducing the northward transport of heat, the AMOC weakening causes a redistribution of heat from high latitude to low latitude. Within the Arctic Ocean, the propagation of heat anomalies is influenced by broadening of cyclonic circulation in the east and weakening of anticyclonic circulation in the west. On the model-mean, the Arctic Ocean warming is most pronounced in the Eurasian Basin, with large spread across the AOGCMs, and accompanied by subsurface cooling by diapycnal mixing and heat redistribution by mesoscale eddies.

## 1 Introduction

Atmosphere–ocean general circulation models (AOGCMs) are widely used for projections of future changes in ocean circulation, heat transport and uptake, includ-

Oleg Saenko
E-mail: oleg.a.saenko@gmail.com

[1] *SEOS, University of Victoria, Victoria, BC, Canada*
[2] *NCAS, University of Reading, Reading, UK*
[3] *Met Office Hadley Centre, Exeter, UK*
[4] *ESSE, York University, Toronto, ON, Canada*

ing in the subpolar and polar regions of the Northern Hemisphere (e.g., Vavrus et al., 2012; Koenigk and Brodeau, 2014; Burgard and Notz, 2017; Nummelin, et al., 2017; Oldenburg et al., 2018; Årthun et al., 2019; Khosravi et al., 2022). One of the more intriguing findings from some of these studies is that, even though the Atlantic meridional overturning circulation (AMOC) weakens with increasing atmospheric $CO_2$ concentration, the ocean heat transport to the Arctic increases (e.g., Koenigk and Brodeau, 2014; Nummelin, et al., 2017; Burgard and Notz, 2017; Oldenburg et al., 2018; Årthun et al., 2019; Yang and Saenko, 2012). The associated increase in the Arctic ocean heat content (OHC) can have major implications for surface climate (e.g., Holland and Bitz, 2003; Nummelin, et al., 2017), sea ice cover (e.g., Koenigk and Brodeau, 2014; Årthun et al., 2019) and sea level rise in the region (e.g., Gregory et al., 2016; Couldrey et al., 2021). It has been shown that one of the main causes of the increased heat transport to the Arctic Ocean under increasing $CO_2$ is related to warmer temperatures of the northward flowing Atlantic waters (Koenigk and Brodeau, 2014; Oldenburg et al., 2018). In the subpolar North Atlantic, the warming of these waters is enhanced by decreased heat loss to the atmosphere (Nummelin et al., 2017). The latter is due, at least in part, to the cooling of sea surface temperature due to the AMOC weakening. The reduction of heat loss from the North Atlantic further weakens the AMOC (Garuba and Klinger, 2016; Gregory et al., 2016; Couldrey et al., 2021). The gyre circulation in the northern North Atlantic and the associated heat transport have also been noted as important contributors to the Arctic Ocean warming (e.g., Jungclaus et al., 2014; Oldenburg et al., 2018; van der Linden et al., 2019).

Several approaches have been used to explore the mechanisms of Arctic Ocean warming under increasing $CO_2$ in the atmosphere. In some studies, the advective component of ocean heat transport is separated into contributions from changes in ocean velocity, temperature, and combinations thereof (e.g., Koenigk and Brodeau, 2014; Oldenburg et al., 2018). The advective ocean heat transport is also sometimes decomposed into overturning and gyre components (e.g., Yang and Saenko, 2012; Jungclaus et al., 2014; Oldenburg et al., 2018; van der Linden et al., 2019). Gregory et al. (2016) and Couldrey et al. (2021) use an ensemble of AOGCMs from the Flux-Anomaly-Forced Model Intercomparison Project (FAFMIP; Gregory et al., 2016) to separate the contributions of added heat and redistributed heat to the OHC change, including in the Arctic Ocean. Nummelin et al. (2017) estimate heat convergence in the Arctic Ocean from the difference between the ocean heat content tendency and surface heat flux in an ensemble of models from the Coupled Model Intercomparison Project phase 5 (CMIP5); a similar approach is applied by Burgard and Notz (2017).

In this study, we aim to investigate several aspects of the Arctic Ocean warming in response to increasing $CO_2$ using the methods described in section 2. In section 3 we present a further separation of the processes contributing to the warming. Unlike in previous CMIPs, the diagnostics representing ocean heat convergences due to different dynamical and physical processes have been officially requested for the CMIP6 models (Griffies et al., 2016). We also take advantage of the fact that such a request was made for the CMIP5 models participating in FAFMIP (Gregory et al., 2016; see also section 2). The availability of detailed heat budget diagnostics makes it possible to estimate the net oceanic heat convergence without the need to compute it as a residual between the surface heat flux and temperature tendency (as in Nummelin et al., 2017, and Burgard and Notz, 2017). It also provides us with an opportunity to further separate the net oceanic heat convergence into contributions from different-scale ocean processes (large-scale ocean circulation, mesoscale eddy effects and small-scale mixing) and estimate the associated uncertainties. It is shown, in particular, that while the large-scale ocean circulation dominates the increased heat convergence in the Arctic Ocean, mesoscale eddy effects and small-scale mixing contribute substantially to the horizontal and vertical structure of warming in the basin's interior.

In section 4, we investigate the influence of ocean dynamics outside of the Arctic Ocean on the region's warming under increasing atmospheric $CO_2$. Motivated by previous studies (e.g., Yang and Saenko, 2012; Jungclaus et al., 2014; Oldenburg et al., 2018; van der Linden et al., 2019; Årthun et al., 2019), the focus is on the baroclinic overturning and barotropic gyre components of ocean circulation and heat transport in the North Atlantic. Some of these previous studies, while investigating the role of gyre and overturning ocean circulations on the Arctic Ocean warming, are based on individual models. Here, instead, we use an ensemble of AOGCMs and address the following questions: 1) which component, overturning or gyre, dominates the increased heat transport to the Arctic Ocean under $CO_2$ forcing and, importantly, what are the associated spreads across AOGCMs? 2) are there relationships between changes in the ocean overturning and gyre circulations in the North Atlantic and GIN Sea (Greenland, Iceland and Norwegian Seas) and the Arctic OHC change? In section 5 we address the contributions to the Arctic Ocean warming from heat addition and redistribution, using a tracer-based approach similar to that employed in Banks and Gregory (2006), Xie and Vallis (2012), Garuba and Klinger (2016) and Gregory et al. (2016). Our main conclusions and possible future research directions are presented in section 6.

## 2 Methods

We analyze a climate change experiment where atmospheric $CO_2$ concentration increases at 1% $yr^{-1}$ (1pctCO2), along with the corresponding output from a preindustrial control experiment (piControl). Unless stated otherwise, the analysis is based on the AOGCMs in Table 1 and is focused on the mean ocean-climate state corresponding to years 61–80 of 1pctCO2; i.e., the 20-year period centred at the time of atmospheric $CO_2$ doubling. To evaluate the contribution of different-scale ocean processes to the Arctic OHC change, we utilize the process-based heat budget diagnostics (Gregory et al., 2016; Griffies et al., 2016). The net change in local ocean temperature (*All scales*) is partitioned into contributions from the large-scale (or resolved) circulation (*Large*), mesoscale eddy effects (*Meso*; this also includes submesoscale eddy effects if they are represented in a model) and small-scale diapycnal mixing processes (*Small*); i.e.,

$$\underbrace{\partial_t \theta}_{All\ scales} = \underbrace{-\mathbf{u} \cdot \nabla\theta}_{Large} \underbrace{- (\mathbf{u}^* \cdot \nabla\theta + \nabla \cdot \mathbf{J}_\theta^{\mathrm{iso}})}_{Meso} \underbrace{- \nabla \cdot \mathbf{J}_\theta^{\mathrm{dia}}}_{Small} + F\ \delta(z), \tag{1}$$

where $\theta$ is the temperature (conservative or potential), $\mathbf{u}$ represents the resolved ocean currents in the analyzed models, $\mathbf{u}^*$ is the parameterized eddy-induced velocity (Gent and McWilliams, 1990; Griffies, 1998), $-\nabla \cdot \mathbf{J}_\theta^{\mathrm{iso}}$ represents temperature convergence due to isopycnal or isoneutral mixing (Redi, 1982; Griffies et al.,

**Table 1.** Information on the AOGCMs employed in this study for heat budget analysis, with the corresponding climate model intercomparison project (CMIP). The geometric mean grid spacing in the Arctic Ocean ($= \sqrt{A_{i,j}}$, where $A_{i,j}$ is the area of $i, j$ grid cell) averaged north of 75°N (A. res.; km) is also indicated. Marked with $*$ are the AOGCMs which employ displaced pole grids in the ocean. Ocean mesoscale (Meso.) eddy advection (adv.) and diffusion (dif.) are represented with either the formulations in Gent and McWilliams (1990; GM90) and Redi (1982; R82), or the formulation in Griffies (1998; G98); all models employ some form of variable eddy transfer coefficients for mesoscale eddy advection, while for eddy diffusion coefficients they employ either variable ($V$) or fixed ($F$) formulations. The models with a parameterization of submesoscale (Submeso.) ocean eddies use Fox-Kemper et at. (2011).

| AOGCM | A. res. | Meso. adv.; dif. | Submeso. | CMIP | Reference |
|---|---|---|---|---|---|
| ACCESS-CM2$*$ | 36 | G98; G98($F$) | Yes | CMIP6 | Bi et al. (2020) |
| CanESM5$*$ | 50 | GM90; R82($V$) | No | CMIP6 | Swart et al. (2019) |
| CESM2$*$ | 42 | G98; G98($V$) | Yes | CMIP6 | Danabasoglu et al. (2012) |
| GFDL-ESM2M$*$ | 54 | G98; G98($F$) | Yes | CMIP5/6 | Dunne et al. (2012) |
| HadCM3 | 57 | GM90; G98($F$) | No | CMIP5 | Gordon et al. (2000) |
| HadGEM2-ES | 45 | G98; G98($F$) | No | CMIP5 | Johns et al. (2006) |
| HadGEM3-GC31-LL$*$ | 51 | GM90; R82($F$) | No | CMIP6 | Kuhlbrodt et al. (2018) |
| IPSL-CM6A-LR$*$ | 51 | GM90; G98($V$) | Yes | CMIP6 | Boucher et al. (2020) |
| MPI-ESM1.2-LR$*$ | 58 | G98; G98($V$) | No | CMIP6 | Gutjahr et al. (2019) |
| MRI-ESM2.0$*$ | 38 | GM90; R82($F$) | No | CMIP6 | Yukimoto et al. (2019) |

1998; Griffies, 1998), and $-\nabla \cdot \mathbf{J}_\theta^{\mathrm{dia}}$ is temperature convergence due to diapycnal (or vertical) mixing processes and all other effects represented in the models (see Griffies et al., 2016); $F$ is the (scaled by the volumetric heat capacity) surface heat flux, with $\delta(z)$ being the Dirac delta function (assuming ocean surface at $z = 0$). Combining *Large* and *Meso* gives the super-residual transport (*SRT*; Kuhlbrodt et al., 2015; Saenko et al., 2021) – a useful quantity which facilitates comparison between models that parameterize ocean mesoscale eddy effects, such as in the employed AOGCMs, and models where these effects are explicitly resolved. The corresponding CMIP6 variable names are as follows (Griffies et al., 2016; Gregory et al., 2016): *All scales* → temptend; *SRT* → temprmadvect; *Large* → temprmadvect−temppadvect; *Meso* → temppadvect+tempmdiff; *Small* → tempdiff +other, prefixed by "opot" or "ocon" for, respectively, potential or conservative temperature. Note: while the terms in Eq. 1 have units of K s$^{-1}$, the corresponding CMIP6 variables are in W m$^{-2}$. More details on the ocean heat budget diagnostics can be found in Griffies et al. (2016) and Gregory et al. (2016).

The relative role of addition and redistribution of heat for the OHC change is explored using one of the AOGCMs, HadCM3. The approach is similar to those employed in e.g. Banks and Gregory (2006), Xie and Vallis (2012) and Garuba and Klinger (2016). In both 1pctCO2 and piControl, we introduce passive tracers representing added heat ($T_a$) and redistributed heat ($T_r$). In the ocean interior, $T_a$ and $T_r$ are transported in the same way as $\theta$ in eq. 1; $T_a$ is initialized with a zero field, while $T_r$ has the same initial distribution as $\theta$. The surface boundary condition for $T_r$ is $F_{clim}$, both in 1pctCO2 and piControl, where $F_{clim}$ is the climatological surface heat flux calculated from piControl. For $T_a$, the surface boundary condition is $F^{'} = F - F_{clim}$, where $F$ is the surface heat flux either in 1pctCO2 or in piControl. Under this framework, $\theta = T_a + T_r$ is a very good approximation in HadCM3, although not exact due to non-linearities and some other effects.

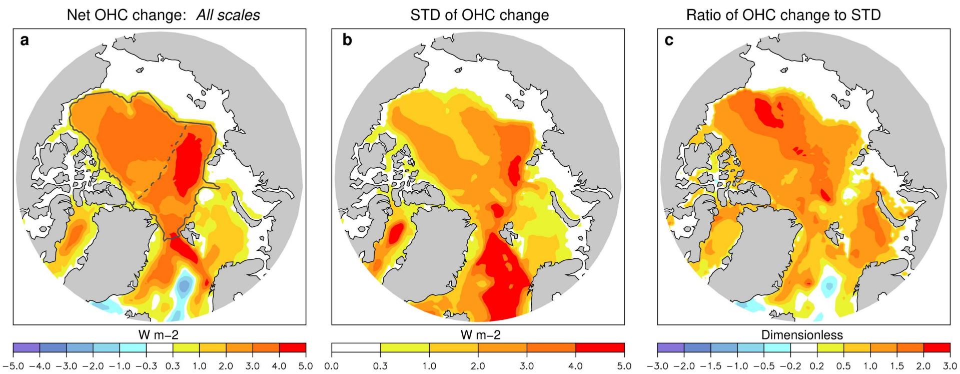


**Fig. 1** Ensemble mean of (a) the Arctic Ocean heat content (OHC) change in 1pctCO2 (relative to piControl) below 100 m depth, (b) its standard deviation (STD) and (c) the ratio of the OHC change in (a) to its STD in (b). The black contour in (a) indicates the Arctic Ocean interior region (with depths typically exceeding 500 m) which is used for a more detailed analysis in the text. An approximate position of the Lomonosov Ridge, separating the Arctic Ocean into the Eurasian Basin and Amerasian Basin, is indicated in (a) with dashed line.

## 3 Physics and dynamics of Arctic Ocean warming

The Arctic Ocean warming is spatially nonuniform (Fig. 1a). In the eastern part of the Arctic Ocean (Eurasian Basin), which is directly influenced by inflow of warm Atlantic Ocean waters, the OHC increases more than in the western part (Amerasian Basin, which includes the Canada Basin, the Makarov Basin and some other basins). Similar patterns of Arctic Ocean warming can be seen in Nummelin et al. (2017) and Khosravi et al. (2022). However, the spread in the Arctic Ocean warming across the AOGCMs is also larger in the Eurasian Basin (Fig. 1b). The ratio of the OHC change to the corresponding intermodel standard deviation (STD) (Fig. 1c) is within the $1-2$ range in most regions, which illustrates the large uncertainty in the Arctic Ocean warming in response to $CO_2$ (also noted by Khosravi et al., 2022).

Before discussing the contribution of individual processes to the Arctic Ocean warming in Fig. 1a, it is useful to consider some major features of the large-scale ocean circulation in the region and their changes in 1pctCO2. The depth-integrated flow is characterized by a cyclonic circulation in the eastern Arctic and anticyclonic gyre in the western Arctic (Fig. 2a). The cyclonic circulation consists of about 5 Sv of Atlantic inflow (Woodgate et al. (2001) estimate the transport of the boundary current in the Eurasian Basin to be 5$\pm$1 Sv). It penetrates to the Arctic Ocean mostly through the Barents Sea and also along the east side of Fram Strait, and leaves the Arctic along the western side of Fram Strait. The strength of the anticyclonic circulation in the western Arctic, the upper part of which constitutes the Beaufort Gyre, is also about 5 Sv in piControl (Fig. 2a), with quite large spread across the models (Fig. 2c). In 1pctCO2, the cyclonic circulation in the east broadens, deviates from the boundary and penetrates to the Amerasian Basin (Fig. 2b). In contrast, the anticyclonic depth-integrated circulation in the west weakens and its area decreases. The corresponding spread across the models is presented in Fig. 2d.

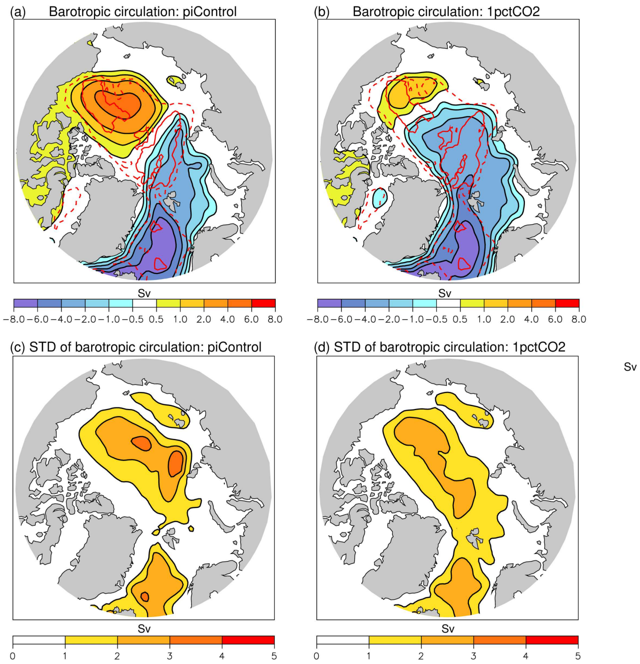


**Fig. 2** Ensemble mean barotropic ocean circulation (Sv; 1 Sv = $10^6$ m$^3$ s$^{-1}$) in the Arctic Ocean in (a) piControl and (b) 1pctCO2, with positive values indicating anticyclonic circulation. The corresponding fields of intermodel standard deviations (STDs) are presented in panels (c) and (d). In panels (a) and (b), also shown are 1,000-m (dashed red) and 3,500-m (solid red) bathymetric contours.

The pattern of wind-stress curl in piControl is characterized by mostly negative values in the Arctic Ocean interior (Fig. 3a). This is consistent with Timmermans and Marshall (2020; their Fig. 2c). Large negative wind-stress curl values in the western Arctic Ocean favour anticyclonic circulation in the region. The area of negative wind-stress curl values somewhat decreases in 1pctCO2, but not the magnitude (Fig. 3b). In fact, the magnitude of negative wind-stress curl somewhat increases in the western Arctic Ocean interior in 1pctCO2, possibly due to decreased sea-ice thickness and cover. It therefore appears that the changes in the depth-integrated circulation in the Arctic Ocean (Fig. 2b) are more due to changes in the ocean's thermohaline structure in 1pctCO2, including due to the (non-uniform) Arctic Ocean warming (Fig. 1a), than due to changes in the winds[1].

The spatial structures of individual processes contributing to the Arctic Ocean heat balance below 100 m depth (i.e., mostly outside of the shelf regions) in piControl and its change in 1pctCO2 are presented in Fig. 4. It is evident that the

[1] From the linear vorticity balance $J(\psi, f/H) = curl(\tau/H) + JEBAR$ (e.g., Mellor, 1999), where $J$ is the Jacobian operator, $f$ is the Coriolis parameter and $H$ is the bottom relief, it follows that the streamfunction of vertically integrated flow ($\psi$) can be forced to cross $f/H$ contours, such as for example those associated with the Lomonosov Ridge, by the curl of wind-stress scaled by $H$ ($curl(\tau/H)$) and by the joint effect of baroclinicity and bottom relief ($JEBAR$; Sarkisyan and Ivanov, 1971). The former can be affected by near-surface winds and sea-ice retreat, while the latter can change due to non-uniform changes in ocean density.

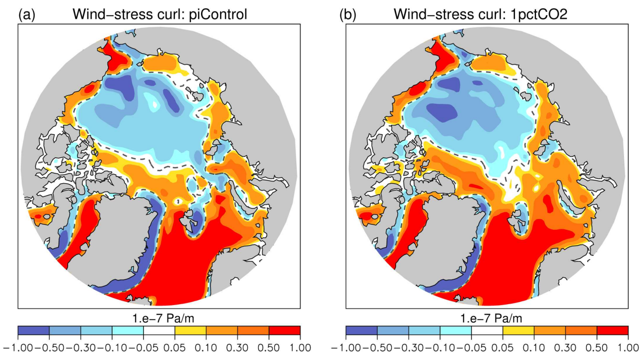


**Fig. 3** Ensemble mean wind-stress curl ($10^{-7}$ Pa m$^{-1}$) in the Arctic Ocean in (a) piControl and (b) 1pctCO2. The dashed contour corresponds to zero wind-stress curl. The curl is calculated from the boundary fluxes of momentum that quantify the net momentum imparted to the liquid ocean surface arising from the overlying atmosphere, sea ice, icebergs, ice shelf, etc. (see Griffies et al., 2016, for more details).

intensity of these processes is typically weaker in the Arctic Ocean than in the GIN Sea. This is expected, since the GIN Sea is a region of strong vertical mixing associated with a large heat loss to the atmosphere, which in a steady state must be balanced by an equally large ocean heat convergence.

Focusing on the Arctic Ocean, it can be seen that, in piControl, cooling of the subsurface interior through small-scale vertical mixing tends to be concentrated along the shelf break regions (Fig. 4a). (Interestingly, Rippeth and Fine, 2022, discuss some observational evidence for enhanced mixing-driven cooling of the Atlantic waters along the Arctic Ocean shelf break.) This cooling is closely balanced by warming from *SRT*; i.e., the combined effect of large-scale and mesoscale processes (Fig. 4b), as expected in a steady state and follows from Eq. 1 below the surface when $\partial_t \theta \rightarrow 0$. The general structure of the net heat transport, which is concentrated along the continental slope and also above the Lomonosov Ridge (Fig. 4b), is broadly consistent with the schemes of Arctic Ocean heat advection based on observational data (e.g., Woodgate et al., 2001; Dmitrenko et al., 2008).

Further partitioning *SRT* into contributions from large-scale advection and mesoscale effects is presented in Fig. 4c,d. It shows positive heat advection by *Large* in the Barents Sea, along the eastern side of Fram Strait and further into the Arctic Ocean along the continental slope (Fig. 4c). *Meso*, through slumping of isopycnals, removes some of this heat from the continental slope regions and deposits it towards the interior, mostly just off continental slope (Fig. 4d). The latter process is offset by *Large*, implying that the large-scale flow deviates from isotherms (i.e. $\int \mathbf{u} \cdot \nabla\theta \; dz \neq 0$) under different angles along the shelf break and in the Arctic Ocean interior. In piControl, this *Large*–*Meso* near compensation in the boundary–interior heat exchange tends to be confined to the upper 500 m layer. Overall, the main mechanism of the Arctic Ocean heat budget in piControl involves heat transport to the basin by *Large*, mostly along the continental slope, heat redistribution by *Meso* and heat flux to the surface by *Small*, followed by its loss to the atmosphere.

In 1pctCO2, the Arctic Ocean is warmed by the joint influence of large-scale heat advection and mesoscale eddy effects; i.e., by *SRT* =*Large*+*Meso* (Fig. 4f).

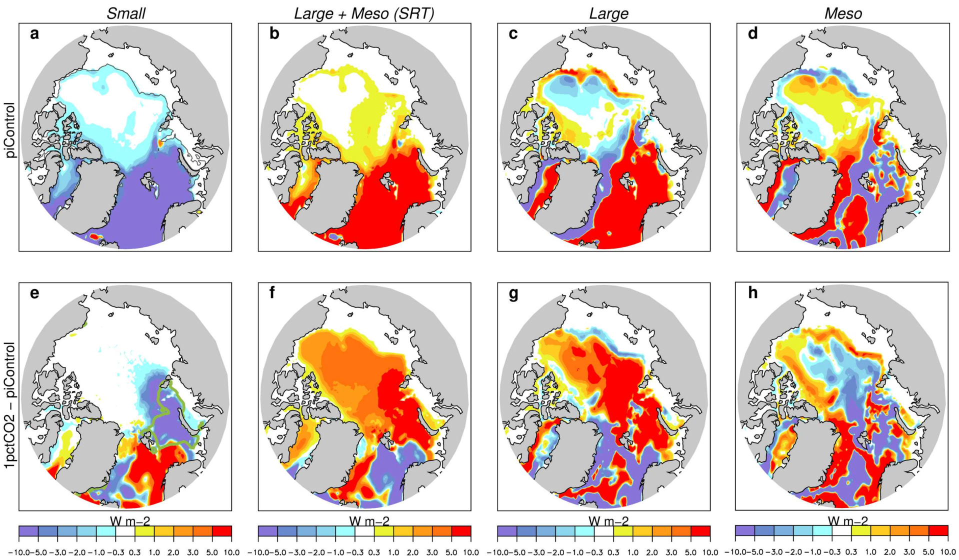


**Fig. 4** Partitioning of the model ensemble-mean rate of change of Arctic Ocean heat content (W $m^{-2}$) below 100 m depth, in (a-d) piControl and (e-h) 1pctCO2 relative to piControl, into contributions due to (a,e) small-scale diapycnal mixing (*Small*), (b,f) the super-residual transport (*SRT = Large + Meso*), (c,g) the resolved large-scale ocean circulation (*Large*) and (d,h) all mesoscale and submesoscale eddy-related processes (*Meso*). The colour scale is limited to ± 10 W $m^{-2}$ for plotting purposes. Positive values correspond to heat being added to the region deeper than 100 m, whereas a negative number indicates cooling below 100 m. The thin black contour in (a) indicates the 100 m isobath, roughly corresponding to the shelf break region, while the thick green contour in (e) indicates the region where the ensemble mean surface heat loss by the ocean in 1pctCO2 (relative to piControl) increases by more than 10 W $m^{-2}$. Note: the net warming in 1pctCO2 (relative to piControl) represents the sum of large positive/negative signals in panels (e) and (f), and so it is shown on a different colour scale in Fig. 1a.

*Large* warms the Arctic Ocean interior, mostly in Eurasian Basin (Fig. 4g). Some of the warming associated with *Large* penetrates to the Amerasian Basin through the central Arctic, deviating from the continental slope. This appears to be related, at least in part, to the changes in the Arctic Ocean large-scale circulation, in particular to the broadening of cyclonic circulation in the east and its deviation from the boundary (Fig. 2b). Khosravi et al. (2022) also note (based on their analysis of ocean temperature structure in the CMIP6 models under two climate change scenarios) that the warming signal propagates from the Eurasian Basin to the Canadian Basin cyclonically, but more through the central Arctic rather than along the boundary current. *Meso* mostly acts to redistribute the extra heat inside the basin, offsetting some of the warming due to *Large* in the Arctic Ocean interior. The removal of heat from the boundary regions by *Meso* weakens (Fig. 4d,h), possibly due to increased stratification which tends to decrease the slope of isopycnals.

Changes in diapycnal mixing (*Small*) act to cool the eastern Arctic Ocean (Fig. 4e). This subsurface cooling is favoured by the locally enhanced surface heat loss, the area of which is indicated by the green contour in Fig. 4e. The persistence of surface and subsurface cooling in the eastern Arctic Ocean enhances heat convergence in the region, mostly due to large-scale heat advection (Fig. 4f,g). This is consistent with Koenigk and Brodeau (2014) who show that the Barents Sea plays an important role in transporting heat to the Arctic Ocean, with some of the heat being lost locally to the atmosphere. Rippeth and Fine (2022) discuss some observational evidence of changing mixing patterns in the eastern Arctic Ocean. They note that the decline of sea ice cover during the past couple of decades has led to increased ocean-atmosphere coupling, with potential for enhancement of turbulent mixing in the eastern Eurasian basin. In contrast, in the GIN Sea there are vast areas where the weakened small-scale mixing, including due to partly suppressed convection (Saenko et al., 2021), leads to subsurface warming by *Small* (Fig. 4e), which tends to be compensated by cooling due to changes in *Large* and *Meso* (or *SRT*; Fig. 4f). In this regard, it is interesting to note that Stouffer et al. (2006), in their North Atlantic freshwater hosing experiments, find a northward shift of the sites of surface heat loss and ocean deep convection from the GIN Sea to the Barents Sea, and the resulting increase in the northward heat transport in the high latitudes of the North Atlantic (their Fig. 8).

The vertical structure of heat balance in the Arctic Ocean region deeper than 500 m (see Fig. 1a) is presented in Fig. 5 (the 500-m depth criteria was selected to exclude the Barents Sea and parts of the Kara Sea and to focus on the Arctic Ocean interior). In piControl, the heat convergence due to *SRT* is mostly confined to the upper $\sim$ 1000 m layer and is closely balanced by cooling due to *Small* (Fig. 5a). In most of the upper 1500 m layer, *SRT* is dominated by *Large*. Within the 100–500 m layer there is a sizable contribution from *Meso* to the warming. However, *Meso* mostly acts to redistribute the heat in the Arctic Ocean interior, with its depth-averaged value being small. Partitioning *Meso* further into contributions from the eddy-induced advection and isopycnal diffusion indicates that the former tends to warm the Arctic Ocean interior, while the latter tends to make it colder (not shown).

It should be noted that ocean mesoscale eddies are known to play an important role in setting water column properties, including in the changing Arctic Ocean (e.g., Armitage et al., 2020). AOGCMs, such as those examined in this study, rely on sophisticated parameterizations to represent some mesoscale and submesoscale eddy effects in the ocean. This also applies to the Arctic Ocean where the Rossby radius in the basin's interior is $\sim$ 10–15 km (Nurser and Bacon, 2014; Timmermans and Marshall, 2020). For example, all AOGCMs employed here for heat budget analysis (Table 1) use variable eddy transfer coefficients to represent eddy-induced advection in the ocean (Gent and McWilliams, 1990). Some AOGCMs also include the Fox-Kemper et at. (2011) parameterization of ocean mixed layer eddies (or submesoscale eddies). Still, the accuracy of these eddy parameterizations in the Arctic Ocean remains to be assessed, especially given the large spread across the models.

In 1pctCO2, the vertical structure of the Arctic Ocean heat balance is strongly disrupted (Fig. 5b), with the heat convergence changes being often greater than the corresponding piControl values (Fig. 5a). The net heat anomaly penetrates to 1500 m depth, being largest around 400 m depth, consistent with Vavrus et al. (2012) and Khosravi et al. (2022). Koenigk and Brodeau (2014) also note that most of the heat which is not passed to the atmosphere in the Barents Sea is stored in the Arctic intermediate layer of Atlantic waters. The net warming (*All scales*) is dominated by heat convergence due to *Large* (Fig. 5b), as expected

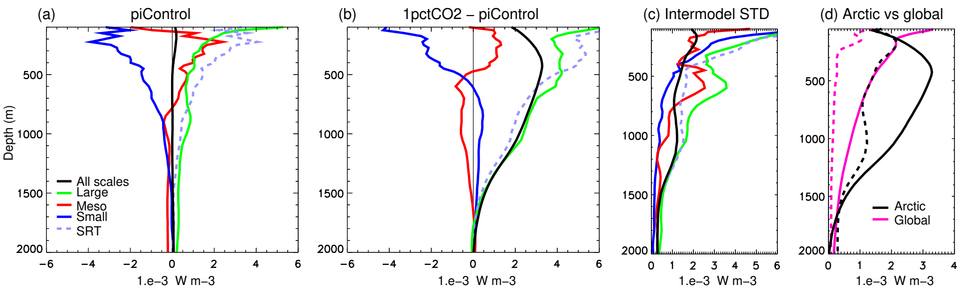


**Fig. 5** (a-c) Ensemble mean profiles of (a) heat convergences in piControl, (b) their changes in 1pctCO2 (relative to piControl) and (c) the intermodel standard deviations for the Arctic Ocean interior region (within the black contour in Fig. 1a). The profiles correspond to the net heating rate (*All scales*, black) and its partitioning into contributions from the resolved large-scale circulation (*Large*, green), all mesoscale and submesoscale eddy-related processes (*Meso*, red) and small-scale diapycnal mixing and all other effects (*Small*, blue); also presented is the superresidual transport (*SRT* = *Large* + *Meso*, dashed gray). (d) The ensemble mean profiles of (solid) net heating rates in 1pctCO2 (relative to piControl) and (dashed) intermodel STDs for (magenta) the global ocean and (black) Arctic Ocean.

from the corresponding horizontal field (Fig. 4g). The warming is enhanced by *Meso* and opposed by *Small* in the upper $\sim$ 500 m layer and vice versa below this depth; *Meso* mostly acts to redistribute the heat. However, the corresponding uncertainties are large (Fig. 5c). The cooling effect of *Small* in the upper 500 m layer (Fig. 5b) is mostly confined to the eastern part of the Arctic Ocean (Fig. 4e). The spread of the Arctic Ocean warming across the models typically increases toward the surface (Fig. 5c). This applies to the net warming rate as well as to the warming rates associated with the individual processes. An exception is the 400–700 m layer where the warming uncertainties in *Large* and *Meso* increase locally. However, the uncertainty in *SRT* does not have this local maximum, indicating that the intermodel warming variations due to changes in *Large* and *Meso* tend to anticorrelate. Also, the spread in *All scales* is smaller than in *Large* and *Meso* above 700 m, and smaller than *Small* above 500 m, implying anticorrelation.

To put the Arctic Ocean warming and its spread across the AOGCMs into context, Fig. 5d compares the profiles of Arctic Ocean warming rate and its intermodel STD with the corresponding profiles for the global ocean. This shows that in the layer below the upper several hundred meters and above 1500 m depth, the rate of the Arctic Ocean warming is about two times larger than that of the global ocean, which is in line with Khosravi et al. (2022). The same applies to the warming spread across the AOGCMs; i.e., the uncertainty of Arctic Ocean warming is much larger than the uncertainty of global ocean warming (Fig. 5d).

## 4 Link to ocean circulation and its changes outside of the Arctic

Bryan's (1982) decomposition of advective ocean heat and freshwater transports into contributions from the overturning and gyre components is part of the CMIP data request (Griffies et al., 2016). While such a geometric decomposition may not always reflect the roles of the corresponding ocean dynamics in transporting heat and freshwater (Saenko et al., 2002), it can provide useful insight into processes acting in the North Atlantic and their links to the Arctic Ocean. Indeed, the decomposition is widely employed in discussions of the mechanisms of heat transport changes in the Arctic Ocean in response to $CO_2$ forcing, most often based on individual models (e.g., Yang and Saenko, 2012; Jungclaus et al., 2014; Oldenburg et al., 2018; van der Linden et al., 2019). We build on these earlier studies to examine both multimodel-mean changes and intermodel spread in the overturning and gyre components of heat transport to the Arctic Ocean. This decomposition also sets the stage for our subsequent analysis of the baroclinic overturning and barotropic gyre circulations in the North Atlantic under increasing $CO_2$ and their relationships with the Arctic OHC change.

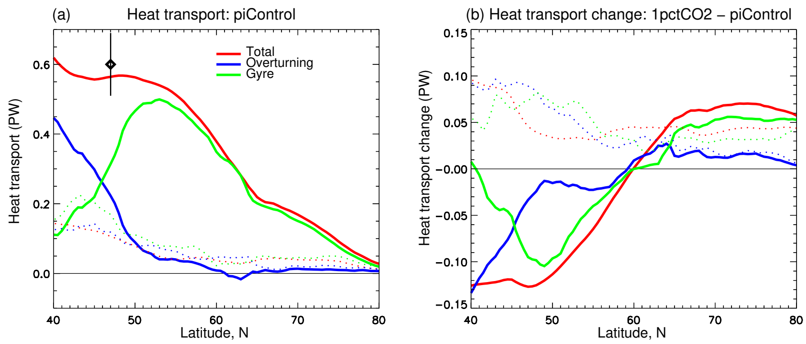


**Fig. 6** (Solid) Ensemble mean (a) northward heat transport in the North Atlantic Ocean in piControl (PW; 1 PW = $10^{15}$ W) and its overturning and gyre components and (b) change in the northward heat transport in the North Atlantic Ocean in 1pctCO2 (relative to piControl) and contribution to the change from the overturning and gyre components. (Dotted) the corresponding intermodel STDs. Also shown in panel (a) is an observational estimate of heat transport at 47°N in the Atlantic Ocean from Ganachaud and Wunsch (2003), with vertical bar indicating its uncertainty. The model data used in constructing this figure is from the following AOGCMs: FGOALS-s2, GISS-E2-1-G, HadGEM3-GC31-LL, HadGEM3-GC31-MM, IPSL-CM6A-LR, MRI-ESM2-0, UKESM1-0-LL, EC-Earth3-CC (see Acknowledgments).

In piControl, the net heat transport in the low-latitude Atlantic Ocean, which is mostly due to heat advection, is dominated by the overturning component. This is because both the vertical temperature contrast and the AMOC strength are strong at these latitudes. Around 45°N, the net northward heat transport is about 0.6 PW, both simulated and observed (Fig. 6a). At these latitudes, the Atlantic Ocean advective heat transport is roughly equally partitioned between the overturning and gyre components, although the corresponding spreads across the models are quite large. North of 50°N, the heat transport is dominated by the gyre component, which is consistent with previous studies (e.g., Grist et al., 2010; Yang and Saenko, 2012; van der Linden et al., 2019). This is because the strong subpolar gyre circulation acts on a relatively strong zonal temperature contract in the region. For example, it requires some 5 K of temperature contract to maintain 0.5 PW of heat transport, given a 25-Sv strong subpolar gyre circulation (see Fig. 9a). On the other hand, the vertical temperature contrast decreases north of 50°N and, as we discuss in section 4, the vertical flow (deep water formation) begins to play an increasingly large role in the AMOC structure. Closer to the Arctic, as the ocean's thermal structure becomes more homogeneous, the heat transport weakens, being only about 0.1±0.03 PW at 75°N (where the uncertainty corresponds to ±1 intermodel STD). The intermodel spread in the heat transport and its overturning and gyre components also tend to decrease with latitude, although not with the same rate as the transports themselves (Fig. 6a).

In 1pctCO2, the heat transport decreases south of about 60°N, but increases north of this latitude (Fig. 6b), implying increased heat convergence in the Arctic Ocean, in agreement with previous studies (e.g., Nummelin, et al., 2017). The increased heat convergence in the Arctic Ocean is favoured by increased heat divergence through vertical mixing in the eastern part of the Arctic Ocean; i.e., in the region where heat loss from the ocean to the atmosphere strongly increases in response to increasing $CO_2$ (as noted in section 3). At 75°N, the heat transport increase is about 0.07±0.04 PW (where the uncertainty corresponds to ±1 intermodel STD), which is comparable to the heat transport in piControl at this latitude. The increase is dominated by the gyre component (Fig. 6b). The contribution from the overturning component to the heat transport increase is also positive north of 60°N. Both the gyre and overturning heat transport changes have large spreads across the models (Fig. 6b). Interestingly, in their historical climate simulation, Jungclaus et al. (2014) also find that the gyre component dominates ocean heat transport increase at 60–65°N toward the end of the 20th century, with positive contribution from the overturning component.

### 4.1 Link to overturning circulation

The AMOC has a major influence on climate, including through its role in the northward transport of heat. However, its relationship with the Arctic Ocean warming in response to $CO_2$ forcing remains unclear (e.g., see discussions in Nummelin et al. 2017; van der Linden et al., 2019). Nummelin et al. (2017) show that it is a reduction in the subpolar North Atlantic heat loss which enhances ocean heat transport to the Arctic Ocean under increasing $CO_2$ forcing. A substantial fraction of this heat input to the northern North Atlantic could be due to a feedback wherein some initial $CO_2$-induced AMOC weakening tends to cool the region, thereby reinforcing surface heat flux to the northern North Atlantic (or reducing heat loss from it), as was concluded based on some specifically designed model experiments by Gregory et al. (2016), Garuba and Klinger (2016) and Couldrey et al. (2021). For example, in the four AOGCMs employed by Gregory et al. (2016), this feedback nearly doubles the heat input to the subpolar North Atlantic associated with the doubling of $CO_2$; in Garuba and Klinger (2016), it is about 70% of the heat added to the region. In addition, it was found that the $CO_2$-induced changes in ocean circulation, mainly associated with the AMOC weakening, lead to a strong redistributive cooling in the North Atlantic and Arctic Ocean (Gregory et al., 2016; Couldrey et al., 2021; see also section 5). Therefore, the net effect from the AMOC weakening on the Arctic Ocean warming is not easy to foresee.

In piControl, the model-mean AMOC strength at 26°N is 16.0±3.2 Sv (the uncertainty corresponds to ±1 intermodel STD). This is comparable to 17.8 Sv, which is an observational estimate of the mean AMOC strength at 26°N for the 2004–2018 period with interannual STD of about 1.8 Sv (Moat et al. 2020; their Table 1). The ensemble mean AMOC pattern indicates that most of the deep water formation in the Atlantic occurs between about 50°N and 65°N, with some

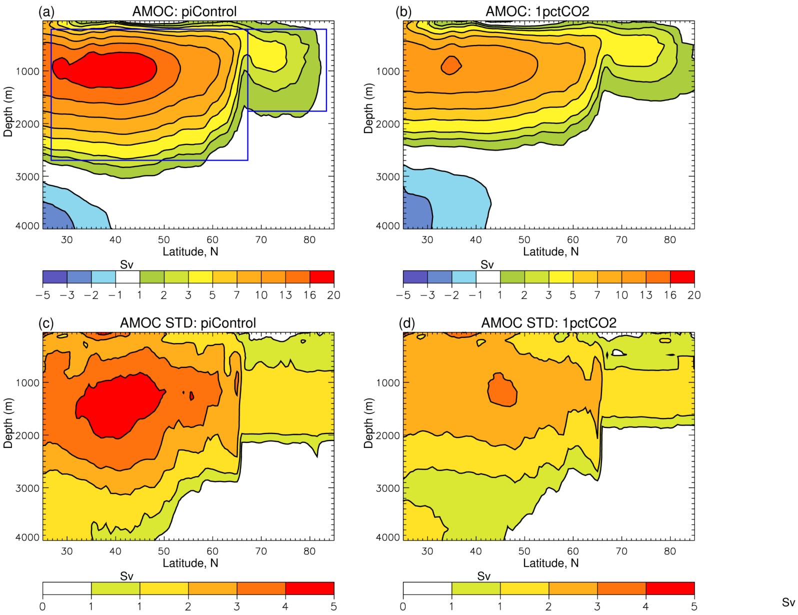


**Fig. 7** Ensemble mean Atlantic meridional overturning circulation (AMOC; Sv; 1Sv = $10^6 m^3 s^{-1}$) in the North Atlantic in (a) piControl and (b) 1pctCO2. The corresponding fields of the AMOC intermodel standard deviations (AMOC STDs; Sv) are presented in panels (c) and (d). The blue boxes in panel (a) indicate the regions of AMOC maximum strength (the mid-latitude AMOC cell) and AMOC extension into the GIN Sea (the GIN Sea overturning cell); these regions are used to calculate the corresponding AMOC strength indexes in Fig. 8.

deep water forming further north in the GIN Sea (Fig. 7a). The AMOC intermodel spread tends to be larger over the latitudes where the AMOC strength is also large (Fig. 7c).

In 1pctCO2, the ensemble mean AMOC strength at 26°N decreases to 12.4±2.5 Sv. This is mostly due to a reduction of deep water formation between 50°N and 65°N, whereas the strength of the AMOC extension north of 65°N remains essentially unaffected (Fig. 7b). Interestingly, the AMOC spread across the models is smaller in 1pctCO2 than in piControl almost everywhere in the North Atlantic (Fig. 7c,d). However, the fractional spread remains roughly the same: the ratio of the piControl AMOC, averaged over the large blue box in Fig. 7a, to its STD in Fig. 7c averaged over the same region is 3.1; the corresponding ratio for the 1pctCO2 AMOC is 3.0.

In models with a larger weakening of the AMOC, the warming of the Arctic Ocean is smaller (Fig. 8a). This relationship between the AMOC change and the Arctic Ocean OHC change appears to arise from the basin-scale heat redistribution, identified in the specifically designed model experiments (Garuba and Klinger, 2016; Gregory et al., 2016; Couldrey et al., 2021; see also section 5): as the AMOC weakens, more heat accumulates in the ocean at the lower latitudes and less heat is redistributed to the higher northern latitudes. As a result, the northern North Atlantic and Arctic Ocean tend to become colder. This redistributive cooling in the north is opposed by heat input at the surface, amplified by a feedback wherein, as the sea surface temperature cools, the heat flux from the

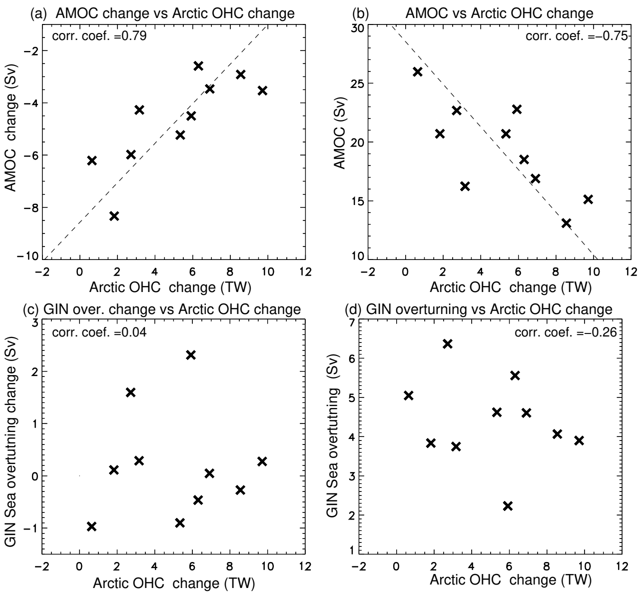


**Fig. 8** Scatter plots of change in the Arctic Ocean heat content in the 100–500m layer (TW; 1TW = $10^{12}$W) in 1pctCO2 (relative to piControl), plotted against (a) change in the strength of the mid-latitude AMOC cell in 1pctCO2 (relative to piControl) and (b) the strength of the midlatitude AMOC cell in piControl (Sv; 1 Sv = $10^6\mathrm{m}^3\mathrm{s}^{-1}$). (c,d) The same as (a,b), except for the GIN Sea overturning cell. The two AMOC overturning cells are indicated with blue boxes in Fig. 7a. As the measure of the overturning strength in each cell we use the maximum value of the baroclinic (overturning) streamfunction in the Atlantic basin. The correlation coefficients (corr. coef.) are also indicated. The dashed lines in panels (a) and (b) correspond to linear regression (see Table 2 for the values of the AMOC strength and its change in each AOGCM).

atmosphere to the ocean increases locally (e.g., Gregory et al., 2016). However, this extra surface heat input to the northern North Atlantic also acts to weaken the AMOC even further, thereby enhancing the redistributive cooling in the north. The net effect of these, and perhaps some other processes, is that the more AMOC weakens, the less heat accumulates in the Arctic Ocean (Fig. 8a).

Interestingly, there is also anticorrelation between the AMOC maximum in piControl and the Arctic Ocean warming in 1pctCO2 (Fig. 8b); i.e., models with larger AMOC maximum in piControl tend to simulate smaller Arctic OHC change in 1pctCO2. However, this anticorrelation seems to arise due to anticorrelation between the AMOC maximum in piControl and the AMOC maximum change in 1pctCO2 (the corresponding correlation coefficient is $-0.65$), which is consistent with previous studies (e.g., Gregory et al., 2005). That is, models with a stronger AMOC tend to produce stronger AMOC weakening. This implies that the spread across the AOGCMs in the piControl AMOC strength indirectly contributes to the spread in the Arctic Ocean warming.

There are no similar relationships between the AMOC extension into the GIN Sea and the Arctic Ocean warming (Fig. 8c,d). Moreover, the models do not show a consistent change in the AMOC extension to the GIN Sea, with the ensemble mean GIN Sea overturning being essentially unaffected (see also Fig. 7). This suggests that at high northern latitudes the contribution of the overturning heat transport to the Arctic Ocean warming arises mostly due to the warmed waters being advected by the (largely unaffected) piControl overturning circulation, consistent with Oldenburg et al. (2018).

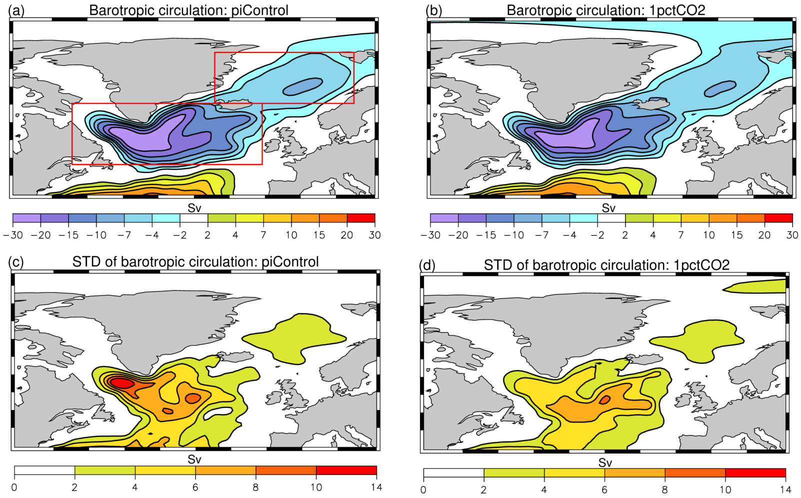


**Fig. 9** Ensemble mean barotropic ocean circulation (Sv; 1 Sv = $10^6$ $m^3$ $s^{-1}$) in the northern North Atlantic in (a) piControl and (b) 1pctCO2. The corresponding fields of intermodel standard deviations (STDs) are presented in panels (c) and (d). Red boxes in panel (a) indicate the subpolar Atlantic and GIN Sea gyres discussed in the text. In models that use free surface methods, the quasi-barotropic streamfunction fields are diagnosed as described in Griffies et al. (2016; eq. H46). These streamfunctions were adjusted here to be equal to zero along the eastern boundary of the Atlantic Ocean.

### 4.2 Link to gyre circulation

The barotropic circulation in the northern North Atlantic is characterized by cyclonic gyres centred in the Labrador Sea (subpolar gyre) and in the GIN Sea (Fig. 9a). On the considered time-space scales, the strength of this circulation is mainly determined by wind-stress curl and bottom pressure torque (e.g., Mellor, 1999). The ensemble mean barotropic circulation is not strongly affected in 1pctCO2 (Fig. 9b). The gyre circulation spread across the models in piControl is similar to that in 1pctCO2 (Fig. 9c,d), except in the Labrador Sea where the spread is larger in piControl. This is because some models simulate a strong barotropic recirculation cell in the north-west Labrador Sea in piControl, while others do not. (This is also why in Fig. 10 we use the barotropic streamfunction averaged over large areas, rather than its minimum, to characterize the gyre strength.)

There is no relationship between the barotropic gyre circulation change in the subpolar North Atlantic and the Arctic OHC change (Fig. 10a). Moreover, the models do not simulate a consistent weakening or strengthening of this gyre in 1pctCO2. The gyre changes do not correlate with the averaged over the subpolar North Atlantic wind-stress curl (not shown), suggesting that bottom pressure

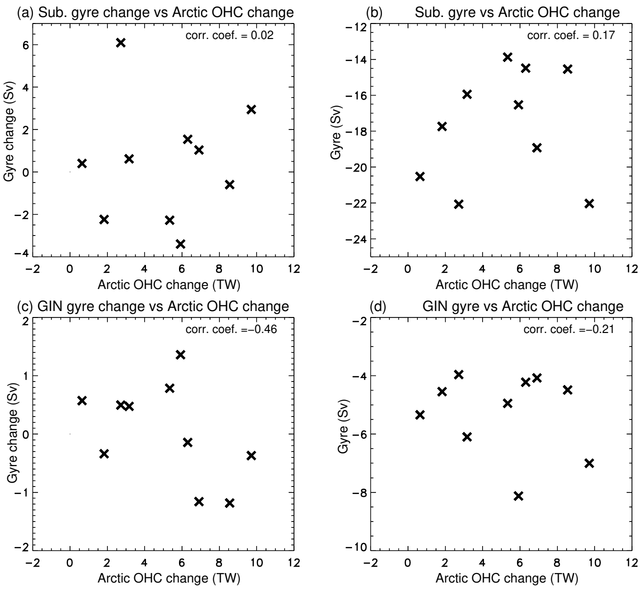


**Fig. 10** Scatter plots of change in the Arctic Ocean heat content in the 100–500m layer (TW; 1TW = $10^{12}$W) in 1pctCO2 (relative to piControl) plotted against (a) change in the subpolar Atlantic gyre strength in 1pctCO2 (relative to piControl) and (b) the subpolar Atlantic gyre strength in piControl (Sv; 1 Sv = $10^6 m^3 s^{-1}$). (c,d) The same as (a,b), except for the GIN Sea gyre. The two gyres are indicated with red boxes in Fig. 9a. As the measure of the gyres strength we use the mean value of the barotropic streamfunction averaged over the regions where the streamfunction is less than $-10$ Sv for the subpolar North Atlantic gyre and less than $-2$ Sv for the GIN Sea gyre. The correlation coefficients (corr. coef.) are also indicated (see Table 2 for the values of the subpolar North Atlantic gyre (SG) strength and its change in each AOGCM).

torques contribute to the gyre changes. Similarly, the relationship between the GIN Sea gyre change and Arctic OHC change is not strong (Fig. 10c), with the AOGCMs being inconsistent in simulating this gyre strength response to the doubling of $CO_2$ in 1pctCO2. Also, there is essentially no relationship between the subpolar gyre strength in piControl and the Arctic Ocean warming (Fig. 10b); the same applies to the GIN Sea gyre strength in piControl (Fig. 10d). This suggests that the increase in the gyre heat transport to the Arctic Ocean at high northern latitudes is more due to warmer ocean temperatures than due to changes in the gyre circulation. The importance of warmer ocean temperatures for the heat transport increase to the Arctic Ocean under different climate change scenarios have been emphasized before (Koenigk and Brodeau, 2014; Nummelin et al., 2017; Oldenburg et al., 2018; van der Linden et al., 2019).

It should also be noted that van der Linden et al. (2019) find that in their model, the baroptopic gyre circulation in the GIN Sea strengthens (becomes more cyclonic; their Fig. 9c) in response to abrupt $CO_2$ quadrupling, thereby contributing to the Arctic Ocean warming. Oldenburg et al. (2018) also note that a strengthened gyre circulation advects warmed surface waters to the Arctic in response to abrupt $CO_2$ quadrupling in their model. Unlike in these studies, we consider a gradual $CO_2$ increase scenario (i.e., 1pctCO2) and focus on the $CO_2$ doubling

**Table 2.** The strengths of AMOC and subpolar North Atlantic gyre (SG) (Sv; 1 Sv = $10^6$ m$^3$ s$^{-1}$) in piControl and their changes in 1pctCO2 relative to piControl ($\Delta$AMOC and $\Delta$SG) in the employed AOGCMs. The measures of the AMOC and SG strengths are defined in the captions to Fig. 8 and Fig. 10, respectively.

| AOGCM | AMOC | $\Delta$AMOC | SG | $\Delta$SG |
|---|---|---|---|---|
| ACCESS-CM2 | 20.7 | -5.2 | -13.9 | -2.3 |
| CanESM5 | 13.1 | -2.9 | -14.5 | -0.6 |
| CESM2 | 22.7 | -6.0 | -22.1 | 6.1 |
| GFDL-ESM2M | 26.0 | -6.2 | -20.1 | 0.4 |
| HadCM3 | 18.5 | -2.6 | -14.5 | 1.5 |
| HadGEM2-ES | 15.1 | -3.5 | -22.0 | 2.9 |
| HadGEM3-GC31-LL | 16.9 | -3.5 | -19.0 | 1.0 |
| IPSL-CM6A-LR | 16.2 | -4.3 | -16.0 | 0.6 |
| MPI-ESM1.2-LR | 22.8 | -4.5 | -16.5 | -3.4 |
| MRI-ESM2.0 | 20.7 | -8.3 | -17.7 | -2.2 |

(rather than quadrupling). Therefore, it is possible that under a stronger $CO_2$ forcing than considered here, or under an abrupt $CO_2$ increase scenario, AOGCMs become more consistent in simulating the GIN Sea gyre response.

## 5 Role of heat addition and redistribution

To obtain further insight on the causes of the Arctic OHC changes under increasing $CO_2$, in particular on the role of AMOC weakening, we analyze the 1pctCO2 and piControl experiments where the OHC change is partitioned into contributions from heat addition and redistribution (see section 2). The experiments were conducted using one of the analysed AOGCMs, HadCM3. While the choice of this model was dictated primarily by its availability to us, we note that it produces heat transport in the Atlantic Ocean and AMOC strength which are reasonably close to observational estimates. In particular, at 47°N in the Atlantic the time-mean ocean heat transport simulated by HadCM3 is 0.57 PW, which is close to the Ganachaud and Wunsch (2003) observational estimate of 0.6±0.09 PW at this latitude. The time-mean AMOC strength at 26°N in HadCM3 is 15.8±1.1 Sv, where the uncertainty corresponds to 1 interannual standard deviation. This is comparable to the AMOC observational estimate at this latitude discussed in subsection 4.1.

In the northern North Atlantic and Arctic, the ocean warming is due to addition of heat, which is opposed by a comparable in magnitude cooling from heat redistribution (Fig. 11a); the contributions from heat addition and redistribution to the meridional structure of thermosteric sea level change are also comparable (not shown). The sum of OHC changes due to heat addition and redistribution (dashed green) closely follows the net OHC change (black), as expected. These results are consistent with the results from the FAFMIP experiments (Gregory et al., 2016; Couldrey et al., 2021). There is a strong relationship between the redistributive cooling in the Arctic Ocean and the AMOC weakening (Fig. 12); the correlation coefficient between the decadal-mean AMOC strength in 1pctCO2 and $\Delta T_r$ north of 75°N is 0.94 (with $\Delta$ denoting the difference between $T_r$ in 1pctCO2 and piControl). There is also a relationship, although less strong, between the AMOC weakening and redistributive warming south of 30°N in the Atlantic Ocean, with

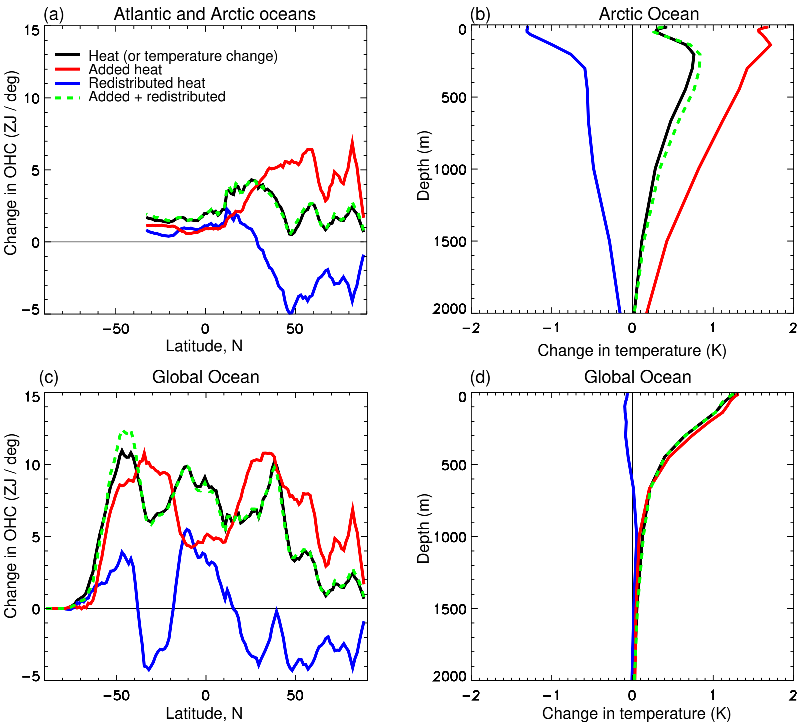


**Fig. 11** Change in (a,c) ocean heat content (OHC; ZJ per degree of latitude; 1 ZJ = $10^{21}$ J) and (b,d) vertical temperature profiles in 1pctCO2 at 2×CO2 (years 61-80) relative to piControl for (a,b) Atlantic and/or Arctic oceans and (c,d) global ocean. Also shown are the contributions to the OHC (or temperature) change from heat addition and redistribution. The figure is based on output from HadCM3 simulations.

the latter confined mostly to the upper ocean. The correlation coefficient between the decadal-mean AMOC strength in 1pctCO2 and $\Delta T_r$ in the 0–500 layer of the Atlantic Ocean within 30°S–30°N is −0.69. These relationships suggest that the AMOC weakening, through this north-south redistribution of heat, acts to mitigate the Arctic Ocean warming (and increase warming in the low-latitude ocean). This supports one of the results in subsection 4.1, that with the AMOC weakening the Arctic Ocean warming tends to decrease (Fig. 8a).

Comparing the Atlantic and Arctic OHC change (Fig. 11a) with the global OHC change (Fig. 11c; cf. Fig. 10 in Gregory et al., 2016) shows that much of the redistributive warming in the global ocean is linked, directly or indirectly, to the redistributive cooling in the northern North Atlantic and Arctic oceans (blue curve in Figs. 11a,c). That is, since heat redistribution must integrate close to zero globally (by the experimental design), then the AMOC-driven heat redistribution and cooling in the North Atlantic (negative values in the blue curve in Fig. 11a) must be compensated by redistributive warming elsewhere (positive values in the blue curve in Fig. 11c).

The vertical structure of $\Delta\theta$ in the Arctic Ocean has comparable in magnitude and opposite in sign contributions from $\Delta T_a$ and $\Delta T_r$ (Fig. 11b). Negative $\Delta T_r$ nearly compensates for positive $\Delta T_a$ in the uppermost Arctic Ocean. This creates

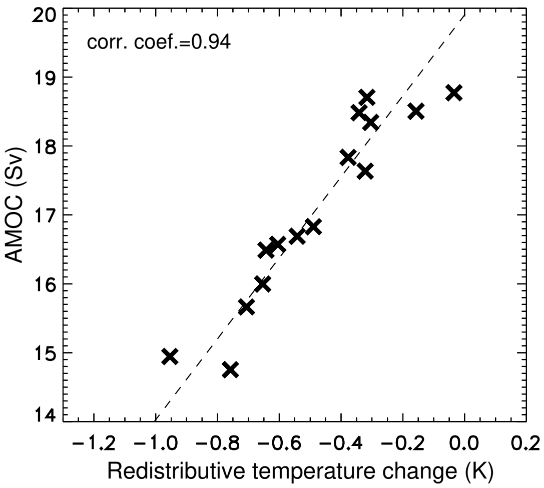


**Fig. 12** The AMOC maximum strength (Sv; 1 Sv = $10^6$ m$^3$ s$^{-1}$) in 1pctCO2 plotted against volume-mean redistributive temperature change ($\Delta T_r$) in 1pctCO2 (relative to piControl) in the Arctic Ocean north of 75°N. The cross symbols correspond to the decadal-mean values of these quantities from the first 150 years of 1pctCO2 (i.e., from the preindustrial $CO_2$ level until it exceeds 4×$CO_2$), while the dashed line is the linear regression. The correlation coefficient (corr. coef.) is also indicated. The figure is based on output from HadCM3 simulations.

a layer of warmest $\Delta\theta$ between about 100 and 1000 m. This contrasts with the global ocean where the influence on the vertical profile of $\Delta\theta$ from $\Delta T_r$ is small (Fig. 11d); only a small fraction of heat is redistributed from the 0–500 layer into the deeper ocean globally. The net warming in the upper 1500 m layer in the Arctic Ocean simulated by HadCM3 is comparable to that in the global ocean (Fig. 11b,d). In contrast, we had previously shown that the multimodel-mean warming in this layer is larger in the Arctic Ocean than in the global ocean (Fig. 5d). However, it should be kept in mind that the vertical warming profile in the Arctic Ocean has a large spread across the AOGCMs.

## 6 Conclusions

We use heat budget diagnostics from an ensemble of AOGCMs, run in preindustrial control (piControl) and an idealized (1pctCO2) climate change experiment, to investigate the contribution of different ocean processes to the warming in the Arctic Ocean interior. In addition, we investigate the links between the Arctic OHC change in 1pctCO2 (relative to piControl) and the baroclinic overturning and barotropic gyre components of the ocean circulation in the North Atlantic. We also address the question of contributions to the Atlantic and Arctic OHC changes from the addition and redistribution of heat. Our main conclusions are as follows:

– In all models, the Arctic Ocean warms under the 1pctCO2 scenario. At doubled $CO_2$, the Arctic Ocean warming is greater than the global ocean warming in the volume mean, and at most depths within the upper 2000 m. The Arctic warming is greatest a few 100 m below the surface.

- The Arctic Ocean warming is dominated by the import of extra heat which is added to the ocean at lower latitudes due to climatic warming. This added heat is conveyed to the Arctic via the subpolar gyre and GIN Sea mostly by the large-scale barotropic ocean circulation. The change in strength of these circulations is relatively small and not correlated with the Arctic Ocean warming.
- The Arctic Ocean warming is opposed and substantially mitigated by the weakening of the AMOC, though the magnitude of this effect has a large intermodel spread. By reducing the northward transport of heat, the AMOC weakening causes a redistribution of heat from high latitudes to low latitudes.
- In the multimodel mean, the Arctic Ocean warming is most pronounced in the Eurasian Basin, with large spread across the AOGCMs, and it is accompanied by subsurface cooling by diapycnal mixing (i.e. upwards, towards the cold sea surface) and heat redistribution by mesoscale eddies (vertically and horizontally).
- The propagation of heat anomalies across the Arctic Ocean is affected by broadening of the depth-integrated circulation in the east and weakening of anticyclonic circulation in the west.

In future studies, it would be helpful to undertake a similar process-based analysis of Arctic Ocean warming based on a multimodel ensemble of AOGCMs where some of the mesoscale eddy effects are explicitly resolved. This would require using ocean model components with rather high resolution, given that the first baroclinic Rossby radius in the Arctic Ocean is $\sim$ 10–15 km in the basin's interior and even smaller in the vast Arctic shelf regions (Nurser and Bacon, 2014; Timmermans and Marshall, 2020); Heuzé et al (2023) report on some improvements in water properties and circulation at eddy-permitting resolution in the Arctic Ocean. It would also be helpful to investigate heat addition and redistribution in other models, using the tracer-based approach applied here.

**Acknowledgements** We thank Matthew Couldrey for comments on an earlier draft. We are grateful to the climate modeling groups for producing and making available their model output, the Earth System Grid Federation (ESGF) for archiving the data and the multiple funding agencies who support CMIP5, CMIP6 and ESGF. The selection of models for Fig. 6 was dictated by availability of the corresponding data in the CMIP5 and CMIP6 archives.

## References

Armitage, T.W., G.E. Manucharyan, A.A. Petty, R. Kwok and A.F. Thompson (2020). Enhanced eddy activity in the Beaufort Gyre in response to sea ice loss. *Nature Communications*, **11**, https://doi.org/10.1038/s41467-020-14449-z.

Årthun, M., Eldevik, T. and L. H. Smedsrud (2019). The role of Atlantic heat transport in future Arctic winter sea ice loss. *J. Climate*, **32**, 3327–3341.

Banks, H. T. and J. M. Gregory (2006). Mechanisms of ocean heat uptake in a coupled climate model and the implications for tracer based predictions of ocean heat uptake. *Geophys. Res. Lett.*, **33**, L07608, doi:10.1029/2005GL025352.

Bi, D., and Coauthors (2020). Configuration and spin-up of ACCESS-CM2, the new generation Australian Community Climate and Earth System Simulator Coupled Model. *Journal of Southern Hemisphere Earth Systems Science*, **70**, 225–251, https://doi.org/10.1071/ES19040.

Boucher, O., and Coauthors (2020). Presentation and evaluation of the IPSL-CM6A-LR climate model. *J. Adv. Model. Earth Syst.*, **12**, e2019MS002010. https://doi.org/10.1029/2019MS002010.

Bryan, K. (1982). Poleward heat transport by the ocean: observations and models. *Annu. Rev. Earth Planet Sci.*, **10**, 15–38.

Burgard, C. and D. Notz (2017). Drivers of Arctic Ocean warming in CMIP5 models. *Geophys. Res. Lett.*, **44**, 4263–4271, doi:10.1002/2016GL072342.

Couldrey, M. P., and and Coauthors (2021). What causes the spread of model projections of ocean dynamic sea level change in response to greenhouse gas forcing? *Climate Dyn.*, **56**, 155–187, https://doi.org/10.1007/s00382-020-05471-4.

Danabasoglu, G., S. C. Bates, B. P. Briegleb, S. R. Jayne, M. Jochum, W. G. Large, S. Peacock and S. G. Yeager (2012). The CCSM4 ocean component. *J. Climate*, **25**, 1361–1389, https://doi.org/10.1175/JCLI-D-11-00091.1

Dmitrenko, I. A., Polyakov, I. V., Kirillov, S. A., Timokhov, L. A., Frolov, I. E., Sokolov, V. T., Simmons, H. L., Ivanov, V. V., and D. Walsh (2008). Toward a warmer Arctic Ocean: Spreading of the early 21st century Atlantic Water warm anomaly along the Eurasian Basin margins. *J. Geophys. Res.*, **113**, C05023, doi:10.1029/2007JC004158.

Dunne, J. P., and Coauthors (2012). GFDL's ESM2 global coupled climate–carbon Earth system models. Part I: Physical formulation and baseline simulation characteristics. *J. Climate*, **25**, 6646–6665, https://doi.org/10.1175/JCLI-D-11-00560.1.

Fox-Kemper, B., G. Danabasoglu, R. Ferrari, S. M. Griffies, R. W. Hallberg, M. Holland, S. Peacock and B. Samuels (2011). Parameterization of mixed layer eddies. III: Global implementation and impact on ocean climate simulations. *Ocean Modell.*, **39**, 61–78, doi:https://doi.org/10.1016/j.ocemod.2010.09.002.

Ganachaud, A. and C. Wunsch (2003). Large-scale ocean heat and freshwater transports during the World Ocean circulation experiment. *J. Climate*, **16**, 696–705.

Garuba, O. and B. Klinger (2016). Ocean heat uptake and interbasin trans- port of passive and redistributive surface heating. *J. Climate*, **29**, 7507–7527, doi:10.1175/JCLI-D-16-0138.1.

Gordon, C., C. Cooper, C. A. Senior, H. T. Banks, J. M. Gregory, T. C. Johns, J. F. B. Mitchell and R. A. Wood (2000). The simulation of SST, sea ice extents and ocean heat transports in a version of the Hadley Centre coupled model without flux adjustments. *Climate Dyn.*, **16**, 147–168.

Gent, P.R. and J. C. McWilliams (1990). Isopycnal mixing in ocean general circulation models. *J. Phys. Oceanogr.,* **20**, 150–155.

Gregory, J. M., and Coauthors (2005). A model intercomparison of changes in the Atlantic thermohaline circulation in response to increasing atmospheric CO2 concentration. *Geophys. Res. Lett.*, **32**, L12703, doi:10.1029/2005GL023209.

Gregory, J. M., and Coauthors (2016). The Flux-Anomaly-Forced Model Intercomparison Project (FAFMIP) contribution to CMIP6: Investigation of sea-level and ocean climate change in response to CO2 forcing. *Geosci. Model Dev.*, **9**, 3993–4017, https://doi.org/10.5194/gmd-9-3993-2016.

Griffies, S. M., 1998: The Gent–McWilliams skew flux. *J. Phys. Oceanogr.*, **28**, 831–841.

Griffies, S. M., A. Gnanadesikan, R.C. Pacanowski, V. Larichev, J.K. Dukowicz and R.D. Smith (1998). Isoneutral diffusion in a z-coordinate ocean model. *J. Phys. Oceanogr.*, **28**, 805–830.

Griffies, S. M., and Coauthors (2016). OMIP contribution to CMIP6: Experimental and diagnostic protocol for the physical component of the Ocean Model Intercomparison Project. *Geosci. Model Dev.*, **9**, 3231–3296, doi:10.5194/gmd-9-3231-2016.

Grist, J. P., and Coauthors (2010). The role of surface heat flux and ocean heat transport convergence in determining the Atlantic Ocean temperature variability. *Ocean Dyn.*, **60**, 771–790, doi:10.1007/s10236-010-0292-4.

Gutjahr, O., Putrasahan, D., Lohmann, K., Jungclaus, J. H., von Storch, J.-S., Brüggemann, N., Haak, H. and A. Stössel (2019). Max Planck Institute Earth System Model (MPI-ESM1.2) for the High-Resolution Model Intercomparison Project (HighResMIP), *Geosci. Model Dev.*, **12**, 3241–3281, https://doi.org/10.5194/gmd-12-3241-2019.

Heuzé, C., Zanowski, H., Karam, S., and M. Muilwijk (2023). The deep Arctic Ocean and Fram Strait in CMIP6 models. *J. Climate*, **36**, 2551–2584, https://doi.org/10.1175/JCLI-D-22-0194.1.

Holland, M. and C. Bitz (2003). Polar amplification of climate change in coupled models. *Climate Dyn.* , **21**, 221–232.

Johns, T. C., and Coauthors (2006) The new Hadley Centre climate model (HadGEM1): Evaluation of coupled simulations. *J. Climate*, **19**, 1327–1353.

Jungclaus, J. H., Lohmann, K. and D. Zanchettin (2014). Enhanced 20th-century heat transfer to the Arctic simulated in the context of climate variations over the last millennium. *Climate of the Past*, **10**, 2201–2213, https://doi.org/10.5194/cp-10-2201-2014.

Khosravi, N., Q. Wang, N. Koldunov, C. Hinrichs, T. Semmler, S. Danilov and and T. Jung (2022). The Arctic Ocean in CMIP6 models: Biases and projected changes in temperature and salinity. *Earth's Future*, **10**, e2021EF002282. https://doi.org/10.1029/2021EF002282.

Koenigk, T. and L. Brodeau (2014). Ocean heat transport into the Arctic in the twentieth and twenty-first century in EC-Earth. *Climate Dyn.*, **42**, 3101–3120. https://doi.org/10.1007/s00382-013-1821-x.

Kuhlbrodt, T., J. M. Gregory and L. C. Shaffrey (2015). A process-based analysis of ocean heat uptake in an AOGCM with an eddy-permitting ocean component. *Climate Dyn.*, **45**, 3205–3226, https://doi.org/10.1007/s00382-015-2534-0.

Kuhlbrodt, T., and Coauthors (2018). The low-resolution version of HadGEM3 GC3.1: Development and evaluation for global climate. *J. Adv. Model. Earth Syst.*, **10**, 2865–2888, https://doi.org/10.1029/2018MS001370.

Mellor, G. (1999). Comments on "On the Utility and Disutility of JEBAR". *J. Phys. Oceanogr.*, **29**, 2117–2118.

Moat, B. I., and Coauthors (2020). Pending recovery in the strength of the meridional overturning circulation at 26°N. *Ocean Sci.*, **16**, 863–874, https://doi.org/10.5194/os-16-863-2020.

Nummelin, A., Li, C. and P. J. Hezel (2017). Connecting ocean heat transport changes from the midlatitudes to the Arctic ocean. *Geophys. Res. Lett.*, **44**, 1899–1908. https://doi.org/10.1002/2016GL071333.

Nurser, A. J. G. and S. Bacon (2014). The Rossby radius in the Arctic Ocean. *Ocean Sci.*, **10**, 967–975.

Oldenburg, D., Armour, K. C., Thompson, L. and C. Bitz (2018). Distinct mechanisms of ocean heat transport into the Arctic under internal variability and climate change. *Geophys. Res. Lett.*, **45**, 7692–7700. https://doi.org/10.1029/2018GL078719.

Redi, M. H. (1982). Oceanic isopycnal mixing by coordinate rotation. *J. Phys. Oceanogr.*, **12**, 1154–1158.

Rippeth, T. P. and E. C. Fine (2022). Turbulent mixing in a changing Arctic Ocean. *Oceanography*, **35**, 66–70. https://doi.org/10.5670/oceanog.2022.103.

Saenko, O.A., J. M. Gregory, A. J. Weaver and M. Eby (2002). Distinguishing the influence of heat, freshwater, and momentum fluxes on ocean circulation and climate. *J. Climate*, **15**, 3686–3697.

Saenko, O.A., J. M. Gregory, S. M. Griffies, M. P. Couldrey and F. B. Dias (2021). Contribution of ocean physics and dynamics at different scales to heat uptake in low-resolution AOGCMs. *J. Climate*, **34**, 2017–2035.

Sarkisyan, A. S. and V. F. Ivanov (1971). Joint effect of baroclinicity and bottom relief as an important factor in the dynamics of sea currents. *Bull. Acad. Sci. USSR, Atmos. and Oceanic Phys.* (English translation), **7**, 173–188.

Stouffer, R.J., and Coauthors (2006). Investigating the causes of the response of the thermohaline circulation to past and future climate changes. *J. Climate*, **19**, 1365–1387.

Swart, N. C., and Coauthors (2019). The Canadian Earth System Model version 5 (CanESM5.0.3). *Geosci. Model Dev. Dis.*, **12**, 4823–4873. https://doi.org/10.5194/gmd-2019-177.

Timmermans, M.-L., and J. Marshall (2020). Understanding Arctic Ocean circulation: A review of ocean dynamics in a changing climate, *J. Geophys. Res.: Oceans*, **125**, e2018JC014378. doi.org/10.1029/2018JC014378.

van der Linden, E. C., Bars, D. L., Bintanja, R. and W. Hazeleger (2019) Oceanic heat transport into the Arctic under high and low CO2 forcing. *Climate Dyn.*, **53**, 4763–4780, https://doi.org/10.1007/s00382-019-04824-y.

Vavrus S., Holland M., Jahn A., Bailey D. and B. Blazey (2012). 21st-century Arctic climate change in CCSM4.*J. Climate*, **25**, 2696–2710, doi:10.1175/JCLI-D-11-00220.1

Woodgate, R. A., K. Aagaard, R. D. Muench, J. Gunn, G. Björk, B. Rudels, A. T. Roach, and U. Schauer (2001) The Arctic Ocean boundary current along the Eurasian slope and the adjacent Lomonosov Ridge: Water mass properties, transports and transformations from moored instruments. *Deep-Sea Res. I*, **48**, 1757–1792, https://doi.org/10.1016/S0967-0637(00)00091-1.

Xie, P. and G. K. Vallis (2012). The passive and active nature of ocean heat uptake in idealized climate change experiments. *Climate Dyn.*, **38**, 667–684, doi:10.1007/s00382-011-1063-8.

Yang, D. and O. A. Saenko (2012). Ocean heat transport and its projected change in CanESM2. *J. Climate*, **25**, 8148–8163, doi:10.1175/JCLI-D-11-00715.1.

Yukimoto, S., and Coauthors (2019). The Meteorological Research Institute Earth System Model version 2.0, MRI-ESM2.0: Description and basic evaluation of the physical component. *J. Meteor. Soc. Japan*, **97**, 931–965, doi:10.2151/jmsj.2019-051.

## Statements and Declarations

**Funding** *The authors declare that no funds, grants, or other support were received during the preparation of this manuscript.*

**Competing Interests** *The authors declare no competing interests.*

**Author Contributions** *OS performed the analysis, produced all the figures and wrote the first draft. JG and NT contributed to the methods design, results analysis and discussions. All authors reviewed the manuscript.*

**Data Availability** *The data used in the study can be obtained from the CMIP5 (`https://esgf-node.llnl.gov/search/cmip5`) and CMIP6 (`https://esgf-data.dkrz.de/projects/cmip6-dkrz/`) data archives.*